Fast Ion Profile Stiffness due to the Resonance Overlap of Multiple Alfvén Eigenmodes

Y. Todo[1,2], M. A. Van Zeeland[3], and W. W. Heidbrink[4]

[1]National Institute for Fusion Science, Toki,Gifu 509-5292, Japan
[2]Department of Fusion Science, SOKENDAI (The Graduate University for Advanced Studies), Toki, Gifu 509-5292, Japan
[3]General Atomics, San Diego, CA 92186-5608, USA
[4]Department of Physics and Astronomy, University of California, Irvine, CA 92697, USA

E-mail: todo@nifs.ac.jp

Abstract. Fast ion pressure profiles flattened by multiple Alfvén eigenmodes are investigated for various neutral beam deposition powers with a multi-phase simulation, which is a combination of classical simulation and hybrid simulation for energetic particles interacting with a magnetohydrodynamic fluid. A monotonic degradation of fast ion confinement and the fast ion profile stiffness are found with increasing beam deposition power. The confinement degradation and the profile stiffness are caused by a sudden increase in fast ion transport flux brought about by Alfvén eigenmodes for the fast ion pressure gradient above a critical value. The critical pressure gradient and the corresponding beam deposition power depend on the radial location. The fast ion pressure gradient stays moderately above the critical value, and the profiles of the fast ion pressure and the fast ion transport flux spread radially outward from the inner region where the beam is injected. It is found that the square root of the MHD fluctuation energy is proportional to the beam deposition power. An analysis of the time evolutions of the fast ion energy flux profiles reveals that intermittent avalanches take place with contributions from the multiple eigenmodes. Surface of section plots demonstrate that the resonance overlap of multiple eigenmodes accounts for the sudden increase in fast ion transport with increasing beam power. The critical gradient and the critical beam power for the profile stiffness are substantially higher than the marginal stability threshold.

PACS numbers: 52.65.Kj, 52.65.Ww, 52.55.Pi, 52.35.Bj

1. Introduction

Alfvén eigenmodes (AEs) are one of the major concerns of burning plasmas because they can transport energetic alpha particles and reduce the alpha heating efficiency leading to deterioration of the plasma performance [1, 2, 3, 4, 5]. Comparison among DIII-D experiments with different beam injection powers revealed the stiffness of the fast ion pressure profile with critical beam powers for sudden increase in fast ion transport flux [6]. In this paper, we regard fast ion profile as "stiff" when the increase of the fast ion profile gradient above a critical value is lower than the proportional increase to the beam power. Critical gradient models based on linear stability analysis have been proposed for the prediction of the fast ion stiff profile[7, 8]. However, we would like to point out that the resonance overlap of multiple eigenmodes [9] can be another mechanism of the critical gradient formation. What is important is that the degree of resonance overlap depends on the mode amplitudes. If the mode amplitudes are not large enough for the resonance overlap, the fast ion flux may not be able to keep the fast ion distribution close to the marginal stability where the fast ion drive is balanced with the intrinsic damping of the modes.

In DIII-D experiments, significant flattening of the fast ion profile was observed during Alfvén eigenmode (AE) activity[10, 11, 12, 13, 14]. In the experiments, a rich spectrum of toroidal Alfvén eigenmodes (TAEs) and reversed shear Alfvén eigenmodes (RSAEs) driven by ∼80keV neutral beam injection is observed during the current ramp-up phase with reversed magnetic shear. Since the fast ion distribution in the DIII-D experiments is significantly affected by AEs, a comprehensive simulation, which deals with both the AEs and the fast ion transport as self-consistently and realistically as possible, yet attainable on a tractable timescale, is needed. We have developed a multi-phase simulation, which is a combination of classical simulation and hybrid simulation for energetic particles interacting with an MHD fluid, in order to investigate a fast ion distribution formation process with beam injection, collisions, losses, and transport due to the AEs [15]. It was demonstrated with the multi-phase simulation of DIII-D discharge #142111 that the fast ion spatial profile is significantly flattened due to the interaction with the multiple AEs and that the fast ion pressure profile is in agreement with that of the experiment with the root-mean-square of the deviations same as the error bar [16]. The predicted temperature fluctuation profiles of $n = 3, 4,$ and 5 modes were quantitatively compared with ECE measurements, and it was found that the fluctuation profiles as well as phase profiles are in very good agreement with the measurements. Additionally, the saturated amplitudes are within a factor of 2 of those measured. The fast ion spatial profile is significantly flattened due to the interaction with the multiple AEs with amplitude $\delta B/B \sim O(10^{-4})$, which is consistent with Refs. [17, 18] where resonance overlap of multiple AEs [9] was found to be the key mechanism for fast ion transport. The nonlinear MHD effects [19, 20, 21, 22, 23] that prevent the AE amplitude from increasing to a large amplitude observed in a reduced simulation [24] are included in the hybrid simulation.

In the present work, we investigate the fast ion pressure profile and the fast ion transport flux brought about by AEs for different beam deposition powers in order to clarify how the fast ion pressure profile and the fast ion transport vary with increasing beam deposition power. We perform a scan of the beam deposition power using the same simulation model and the equilibrium data as used in Ref. [16].

2. Simulation model

We use the MEGA code [25], in which the bulk plasma is described by the nonlinear MHD equations and the fast ions are simulated with the particle-in-cell method. In this work, we use the same MHD model as used in our previous work [16] where an extended MHD model given in Ref. [26] is employed, and the equilibrium toroidal flow is taken into account. The extended MHD equations with the fast ion effects are given by

$$\frac{\partial \rho}{\partial t} = -\nabla\cdot(\rho\mathbf{v}_{\rm H}) + \nu_n\triangle(\rho-\rho_{eq}), \tag{1}$$

$$\rho\frac{\partial}{\partial t}\mathbf{v} = -\rho\mathbf{v}_{\rm H}\cdot\nabla\mathbf{v} + \rho\mathbf{v}_{\rm pi}\cdot\nabla(v_\parallel\mathbf{b}) - \nabla p + (\mathbf{j}-\mathbf{j}_h')\times\mathbf{B} + \frac{4}{3}\nabla(\nu\rho\nabla\cdot\mathbf{v}) - \nabla\times(\nu\rho\boldsymbol{\omega}), \tag{2}$$

$$\frac{\partial p}{\partial t} = -\nabla\cdot[p(\mathbf{v}+\mathbf{v}_{\rm tor})] - (\gamma-1)p\nabla\cdot[\mathbf{v}+\mathbf{v}_{\rm tor}] + (\gamma-1)\left[\nu\rho\omega^2 + \frac{4}{3}\nu\rho(\nabla\cdot\mathbf{v})^2 + \eta\mathbf{j}\cdot(\mathbf{j}-\mathbf{j}_{eq})\right] + \chi\triangle(p-p_{eq}), \tag{3}$$

$$\frac{\partial \mathbf{B}}{\partial t} = -\nabla\times\mathbf{E},\ \mathbf{j} = \frac{1}{\mu_0}\nabla\times\mathbf{B}, \tag{4}$$

$$\mathbf{E} = -\mathbf{v}_E\times\mathbf{B} - \mathbf{v}_{\rm tor}\times(\mathbf{B}-\mathbf{B}_{eq}) + \eta(\mathbf{j}-\mathbf{j}_{eq}), \tag{5}$$

$$\mathbf{v}_{\rm H} = \mathbf{v}+\mathbf{v}_{\rm pi}+\mathbf{v}_{\rm tor},\ \mathbf{v}_{\rm pi} = -\frac{m_i}{2e_i\rho}\nabla\times\left(\frac{p\mathbf{b}}{B}\right), \tag{6}$$

$$v_\parallel = \mathbf{v}\cdot\mathbf{b},\ \mathbf{v}_E = \mathbf{v}-v_\parallel\mathbf{b},\ \boldsymbol{\omega} = \nabla\times\mathbf{v} \tag{7}$$

where μ_0 is the vacuum magnetic permeability, γ is the adiabatic constant, and ν, ν_n and χ are artificial viscosity and diffusion coefficients chosen to maintain numerical stability. In this work, the dissipation coefficients ν, ν_n, χ, and η/μ_0 are assumed to be equal to each other. The dissipation terms (viscosity, resistivity, and diffusivity) play a physical role to enhance the damping of AE modes in the MHD simulation that includes continuum damping [27, 28] but does not include kinetic damping such as radiative damping [29] and thermal ion Landau damping. In this paper, we use the same value of the coefficients as used in the previous work, 5×10^{-7} normalized by v_AR_0 where v_A is the Alfvén velocity at the plasma center, and R_0 is the major radius at the geometrical center of the simulation domain. The subscript "eq" represents the equilibrium variables. The equilibrium toroidal flow velocity $\mathbf{v}_{\rm tor}$, which is assumed to

Table 1. Beam deposition power (P_{NBI}), the last hybrid simulation period ($t_s - t_e$), beam injection period (t_{inj}), and number of particles (N).

P_{NBI} [MW]	1.56	3.13	4.69	6.25	7.81	9.38	12.5	15.6
$t_s - t_e$ [ms]	90-92	76-78	70-72	70-72	60-62	60-62	55-57	55-57
t_{inj} [ms]	100	150	150	150	75	100	75	75
N [10^6]	4.2	8.4	8.4	8.4	4.2	4.2	4.2	4.2

be constant in time, and the thermal ion diamagnetic drift velocity $\mathbf{v}_{\rm pi}$ are included in the equations. For the thermal ion diamagnetic drift velocity given by Eq. (6), we retain only the magnetization current part and neglected the remaining part that corresponds to the grad-B and curvature drift in order to keep the initial density profile in equilibrium. Otherwise, the density profile would evolve and deviate from the initial profile and become non-uniform on magnetic surface. The MHD momentum equation [Eq. (2)] includes the fast ion contribution in the fast ion current density $\mathbf{j}'_h$ that consists of the contributions from parallel velocity, magnetic curvature and gradient drifts, and magnetization current. The $\mathbf{E}\times\mathbf{B}$ drift disappears in $\mathbf{j}'_h$ due to the quasi-neutrality [25]. The fast ions are simulated using the full-f particle-in-cell (PIC) method, and a guiding-center approximation [30], where we employ the gyrokinetic approach to account for finite Larmor radius effects. The electromagnetic fluctuations are averaged over the fast ion gyro orbit for the fast ion dynamics. It was demonstrated that the MEGA code with the full-f PIC method can be applied to energetic particle modes in JT-60U, although the numerical noise level is higher in the full-f PIC simulation than in the delta-f PIC simulation [31, 32]. Cylindrical coordinates (R, φ, z) are used in the simulation. The numbers of grid points are (128, 128, 256) for (R, φ, z) coordinates, respectively. For the purpose of the data analysis, magnetic flux coordinates (r, φ, ϑ) were constructed for the MHD equilibrium where r is the radial coordinate with $r = 0$ at the plasma center and $r = a$ at the plasma edge, and ϑ is the poloidal angle.

3. Simulation results

3.1. Fast ion pressure profile and Alfvén eigenmodes

In our previous work, we ran a multi-phase simulation and a classical simulation for the DIII-D discharge #142111 at t=525ms with beam deposition power 6.25MW [16]. The beam injection energy is approximately 80keV, and the full, half, and third energy components are considered. The ratio of the beam ion velocity with 80keV energy to the Alfvén velocity at the plasma center is 0.50. Collisions (slowing down, pitch-angle scattering, and energy diffusion) and fast-ion losses are included in the simulations. In this work we investigate a total of 8 cases with different beam deposition powers using the equilibrium data and the beam deposition profile that was used in the previous work. The MHD equilibrium was reconstructed with EFIT code [33] assuming the MHD velocity $\mathbf{v} = 0$. The MHD equilibrium is also an equilibrium for Eqs. (1)-

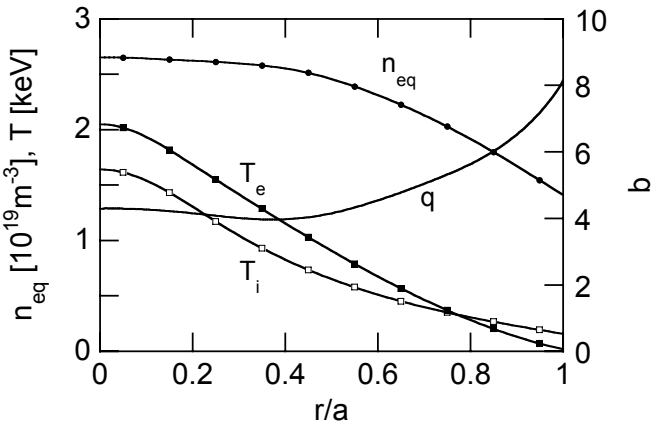

Figure 1. Radial profiles of equilibrium ion density (n_{eq}), electron temperature (T_e), ion temperature (T_i), and safety factor (q).

(7). The equilibrium profiles of ion density ($n_{eq} = \rho_{eq}/m_D$), electron temperature, ion temperature, and the safety factor, where m_D is deuterium mass, are shown in Fig. 1. We use experimental values for collision frequencies. The multi-phase simulations are run with alternating classical phase for 4ms and hybrid phase for 1ms. This combination is repeated until stored fast ion energy is saturated, after which, the hybrid simulation is continuously run for 2ms. Computational particles are injected at a constant rate over a beam injection period t_{inj}, although both the multi-phase and classical simulations are terminated before $t = t_{inj}$. The slowing-down time is 227ms at the plasma center, and the time scale for energy decrease is a half of the slowing-down time. In the previous work, t_{inj} was set to be 150ms, which covers the energy decrease time, but the run was terminated before $t = 75$ms because the stored fast ion energy reached a steady state at $t = 70$ms. In some runs in this work, we reduce the beam injection period t_{inj} to 75 or 100ms. This enables us to reduce the number of particles keeping the numerical particle injection rate similar among the runs. We restrict the toroidal mode number of energetic particle drive in the simulation to $n = 1 - 5$ in order to reduce the numerical noise. This is supported by the experimental observation that the toroidal mode number of

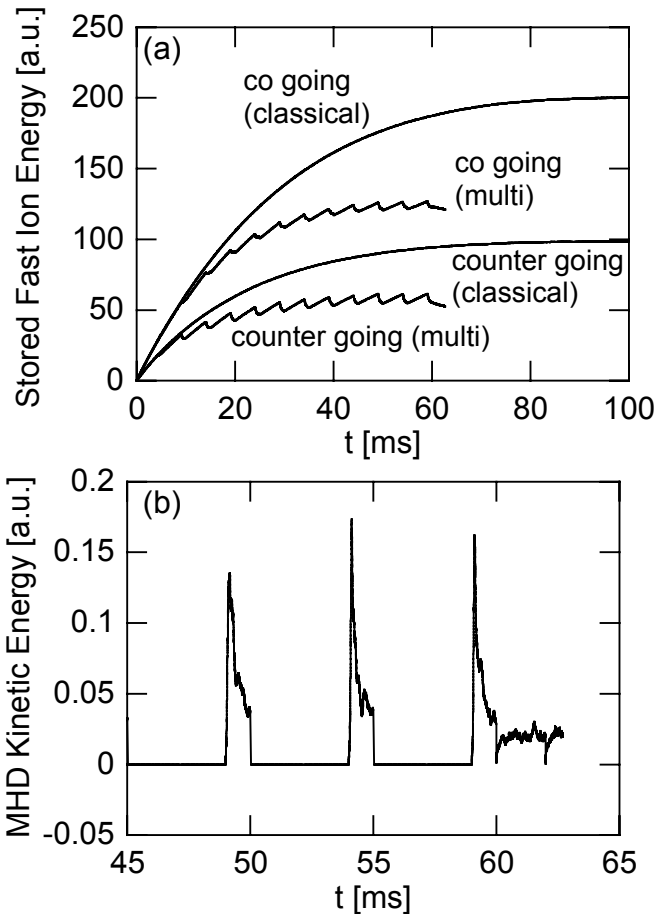

Figure 2. Time evolutions of (a) stored fast ion energy in multi-phase and classical simulations, and (b) MHD kinetic energy in the multi-phase simulation for beam deposition power 9.38MW.

the AE modes is $n = 1-5$ at $t \sim 525$ms [14]. The beam deposition profile is the same as used in the previous work, but the computational particle weight is scaled to match the total deposition power. Table 1 summarizes the beam deposition power, the last hybrid simulation period, the beam deposition period t_{inj}, and the number of computational particles. It was confirmed in a reduced simulation of bursting evolution of five AEs with toroidal mode number $n = 1-5$ that 2 million particles are sufficient for numerical convergence in burst interval, modulation depth of the stored fast ion energy at each burst, and saturation level of the stored fast ion energy [24]. The time evolutions of stored fast ion energy and the MHD kinetic energy are shown for P_{NBI} =9.38MW in Fig. 2. The stored fast ion energy evolutions are compared among the multi-phase simulation and the classical simulation in Fig. 2(a).

Figure 3(a) shows the ratio of stored fast ion energy in the multi-phase simulation to that in the classical simulation for various beam deposition powers. We see a monotonic decrease in the ratio for the higher beam deposition power, which indicates a degradation of fast ion confinement. For the highest beam deposition power, the stored fast ion

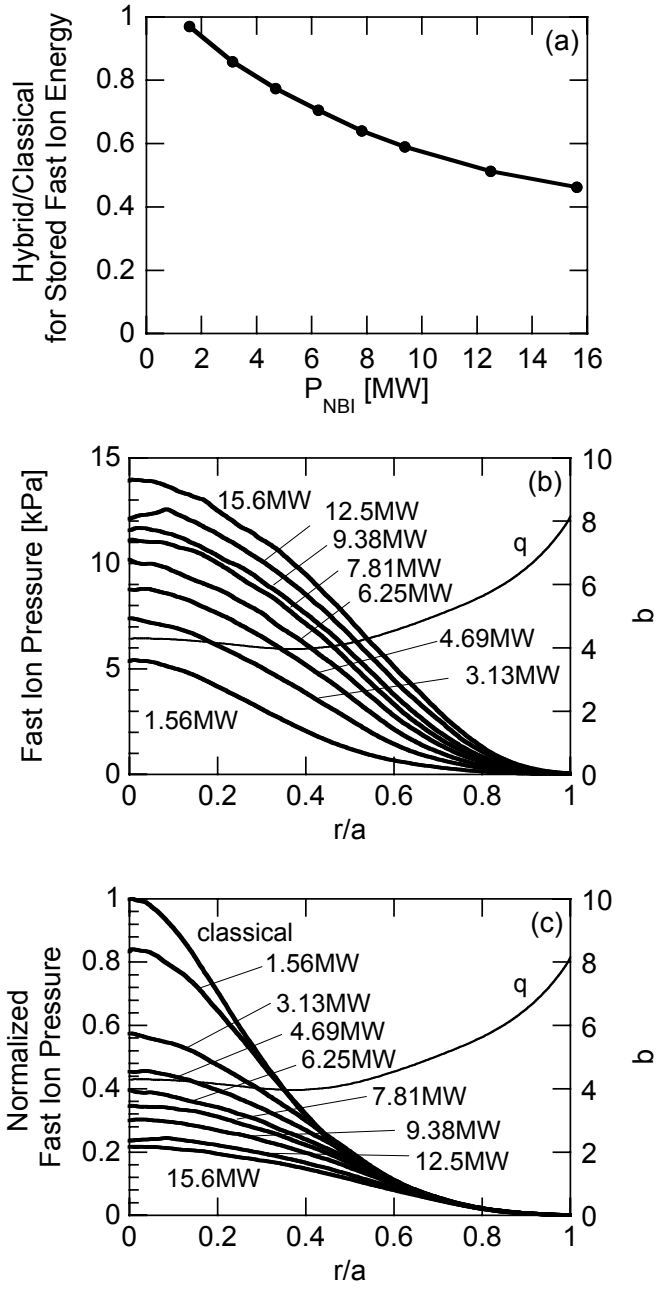

Figure 3. (a) Ratio of stored fast ion energy in multi-phase simulation to that in classical simulation versus beam deposition power, (b) comparison of fast ion pressure profiles, and (c) comparison of fast ion pressure profiles normalized by the central classical pressure among various beam deposition powers.

energy is reduced to 46% of the classical value. Figure 3(b) shows the fast ion pressure profiles at the final time ($t = t_e$) for all the runs. The fast ion pressure increases for the higher beam deposition power. However, the increase is not linearly proportional to the beam deposition power. This is indicated in Fig. 3(c) where the fast ion pressure profiles are normalized by the classical pressure at the plasma center for each run. We see that the normalized fast ion pressure is reduced for the higher beam deposition power, which indicates the profile stiffness. For the highest beam deposition power P_{NBI} =15.6MW, the fast ion pressure in the hybrid simulation is only 22% of that in the classical simulation at the plasma center.

The reduction in stored fast ion energy and fast ion pressure is brought about by the interaction with multiple Alfvén eigenmodes (AEs). The frequencies and the spatial profiles of the AEs are analyzed for the last 2ms of the hybrid phase. The dominant AEs are toroidal Alfvén eigenmodes (TAEs) with toroidal mode number $n = 1 - 5$, which are the same as the run for P_{NBI} =6.25 MW presented in our previous work. The run for P_{NBI} =6.25MW was validated with the DIII-D experiment for the fast ion pressure profile and the electron temperature fluctuation profiles with toroidal mode number $n = 3 - 5$ including the absolute amplitude and the phase profile[16]. The spatial profiles of the TAEs are compared in Fig. 4 between P_{NBI} =1.56MW and 15.6MW. The major poloidal harmonics and the peak locations are the same between P_{NBI} =1.56MW and 15.6MW for all the modes. The ratio of the cosine part to the sine part, which are represented by solid and dashed lines, respectively, in the figure, indicates the phase of each harmonic. We see in Fig. 4(e) that the sign of the cosine part varies from positive for $m = 13$ to negative for $m = 18$ with the sine part negative for $m = 15$. This indicates a smooth variation in the phase of the spatial profile, which corresponds to a sheared spatial profile. This kind of phase variation is weak in Fig. 4(f) for P_{NBI} =15.6MW. Frequencies are lower by 5-10% for the higher beam deposition power P_{NBI} = 15.6MW. Apart from the differences for phase profile and frequency, the modes are almost the same for all the runs. For P_{NBI} =15.6MW, another $n = 2$ mode is found near the plasma edge with frequency 57kHz. This mode is considered in the surface of section plot presented in subsection 3.3.

The width of resonance regions in phase space depends on mode amplitude. The amplitudes of the TAEs are shown versus beam deposition power in Fig. 5(a). We see a rising trend in the $n = 3$ TAE amplitude, which is the largest for most of the runs. The MHD kinetic energy roughly represents the total energy of AEs. The square root of MHD kinetic energy is plotted versus P_{NBI} in Fig. 5(b), which shows a linear increase with beam deposition power. This is similar to the observations in DIII-D experiments where the sum of the AE amplitudes increases with total beam power above a stability threshold[6].

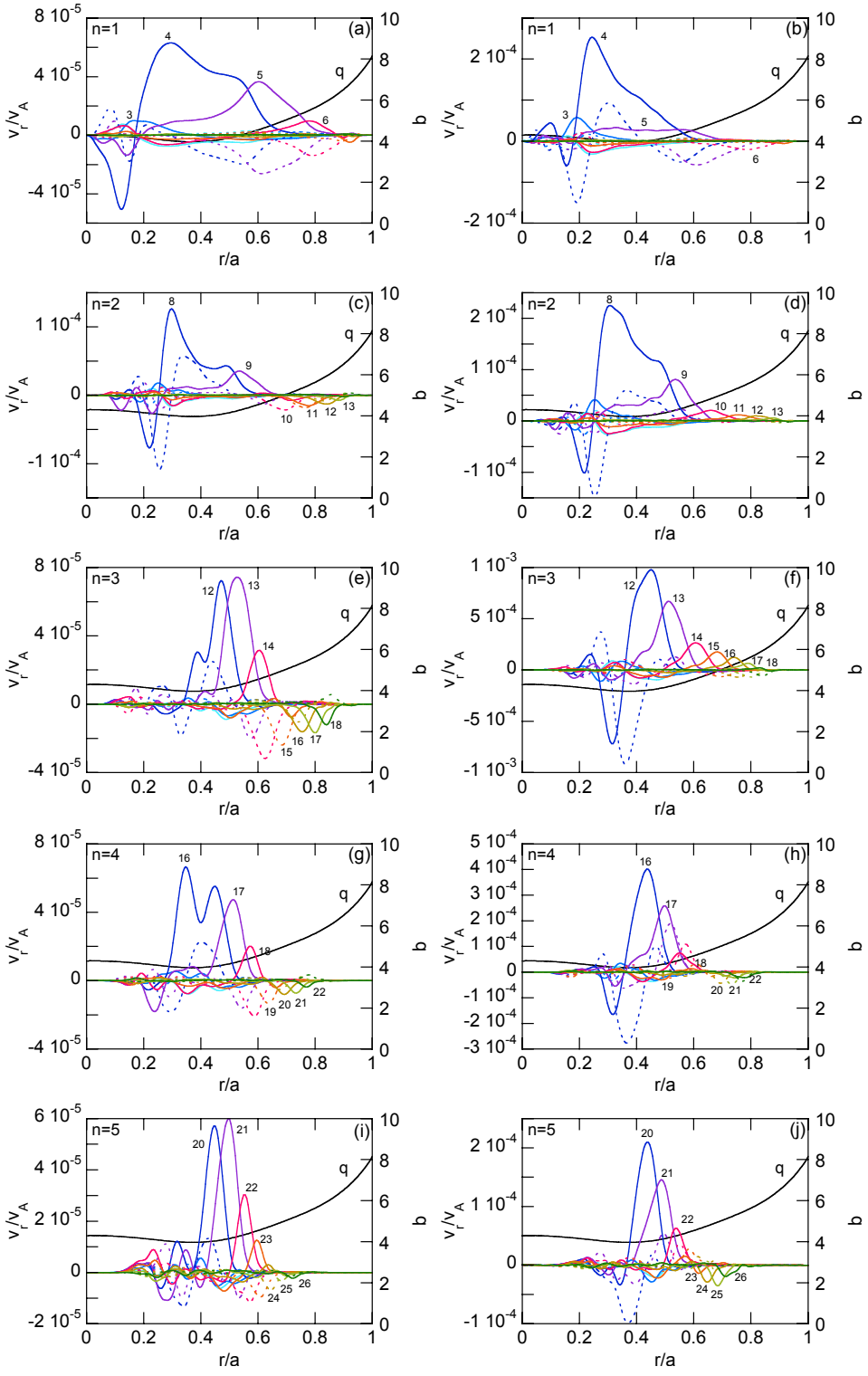

Figure 4. Radial velocity profiles of TAEs for beam deposition power (a), (c), (e), (g), (i) 1.56MW and (b), (d), (f), (h), (j) 15.6MW with toroidal mode number and frequency (a) n=1, 64kHz, (b) n=1, 61kHz, (c) n=2, 68kHz, (d) n=2, 68kHz, (e) n=3, 72kHz, (f) n=3, 67kHz, (g) n=4, 77kHz, (h) n=4, 70kHz, (i) n=5, 81kHz, and (j) n=5, 73kHz. Solid (dashed) lines show $\cos(m\vartheta+n\varphi)$ [$\sin(m\vartheta+n\varphi)$] harmonics with poloidal mode number m labeled in the figure.

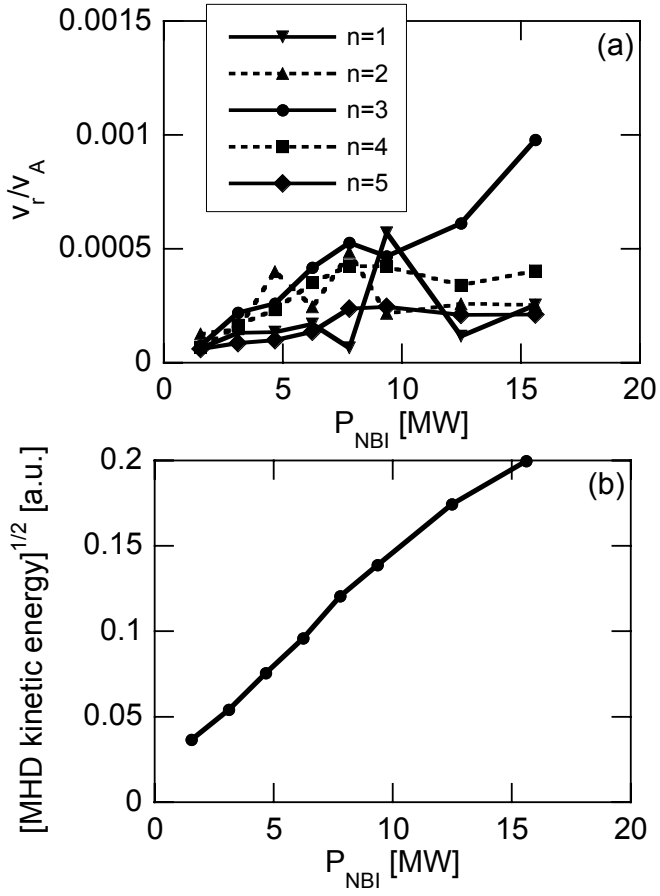

Figure 5. (a) Amplitudes of TAEs with toroidal mode number $n = 1 - 5$ and (b) the square root of MHD kinetic energy versus beam deposition power.

3.2. Critical gradient of fast ion pressure profile

For physical understanding of the fast ion pressure profiles, we have analyzed the spatial gradient of the fast ion pressure profile and the fast ion energy flux brought about by the MHD perturbations. The fast ion energy flux brought about by the MHD perturbations with toroidal mode number n is defined by

$$F_n(r) = \int_0^{2\pi} \mathcal{J}(r,\vartheta)d\vartheta \int_0^{2\pi} d\varphi \frac{1}{2}\left[(P_{\parallel n} + 2P_{\perp n})v_{Ern} + (Q_{\parallel n} + 2Q_{\perp n})\delta b_{rn}\right], \quad (8)$$

where $\mathcal{J}$, $P_\parallel$, $P_\perp$, $Q_\parallel$, $Q_\perp$, v_{Er}, and δb_r are Jacobian, fast ion parallel and perpendicular pressures, parallel and perpendicular 3rd order moments, radial $E \times B$ drift velocity, and radial fluctuation of magnetic field unit vector, respectively. The derivation of Eq. (8) is given in Appendix A.

Figure 6 shows the radial profiles of the fast ion beta gradient and the fast ion energy flux for all the runs. Fast ion beta β_h is the ratio of fast ion pressure to the magnetic pressure, and $\rho = r/a$ is the normalized radius. The profiles averaged in the last 2ms of the hybrid phase are shown in Fig. 6. The fast ion energy fluxes given by Eq. (8) are summed over $n = 1 - 5$. When we compare the fast ion beta gradient profiles between

the lowest (1.56MW) and the highest (15.6MW) beam deposition powers, the maximum value increases by only a factor of 2, and the peak location shifts from $r/a \sim 0.2$ to $r/a \sim 0.5$. This indicates that the increase in fast ion pressure gradient is limited, and that the fast ion pressure profile spreads radially outward. On the other hand, the increase in the fast ion energy flux shown in Fig. 6(b) is remarkable. It should be noted that the figure is normalized by the beam deposition power for each run. Then, the rise in fast ion energy flux for the higher beam deposition power in the figure indicates the rapid increase in the fast ion energy flux.

Let us examine the relations among beam deposition power, fast ion beta gradient, and fast ion energy flux for fixed radii. The fast ion beta gradient is plotted versus beam deposition power for various radii in Fig. 7(a). We see pressure gradient increases for higher beam deposition power. However, the increase is not a linear function of beam deposition power. For $r/a = 0.4$ and $r/a = 0.6$, the increase of beta gradient slows down when the beta gradient reaches $-d\beta_h/d\rho \sim 0.008 - 0.01$. We turn our attention to the relation between the fast ion energy flux and the fast ion pressure gradient. Figure 7(b) shows this relation. We see a sudden increase in fast ion energy flux for $-d\beta_h/d\rho > 0.008$. This rapid increase in fast ion energy flux suppresses the increase in fast ion pressure gradient leading to the stiffness of the fast ion pressure profile. Figure 7(c) shows the fast ion energy flux versus beam deposition power. We see critical beam deposition powers for the sudden increase in fast ion energy flux, $P_{NBI} \sim 3MW$ for $r/a = 0.6$, $P_{NBI} \sim 6MW$ for $r/a = 0.7$, and $P_{NBI} \sim 8MW$ for $r/a = 0.8$. These results are similar to the observations in DIII-D experiments where fast ion transport suddenly begins to increase above a threshold, and the threshold depends on the phase space location on which each measurement focuses [6].

3.3. Time evolution of fast ion energy flux profile and resonance overlap

The fast ion energy flux profile shown in Fig. 6(b) is an average in the last 2ms of the hybrid phase for each run. The time evolution of fast ion energy flux profile and the contribution from each eigenmode to the fast ion transport are useful for our understanding of the fast ion transport mechanism. Figure 8 shows the time evolutions of the total energy flux and the energy flux brought about by each toroidal node number for P_{NBI} =1.56MW, 3.13MW, 6.25MW, and 15.6MW. Figures 8(a), (c), (e), and (g) show the time evolutions of the total energy flux profiles. The energy flux shown in the figure is averaged over 0.02ms. We see intermittent properties in the energy flux evolutions. The time evolution of fast ion energy flux at $r/a = 0.46$ for P_{NBI} =6.25MW is shown in Fig. 9 to clarify the intermittent properties. The large fluxes shown in Fig. 8 look like avalanches propagating radially outward and sometimes inward. Some avalanches are highlighted in Fig. 8(e). For larger beam deposition power, the energy flux profiles spread to the edge. Figures 8(b), (d), (f), and (h) show contours of the energy flux for each toroidal mode number defined by Eq. (8), for which the toroidal mode number is distinguished with color. We see in the figures that the multiple modes

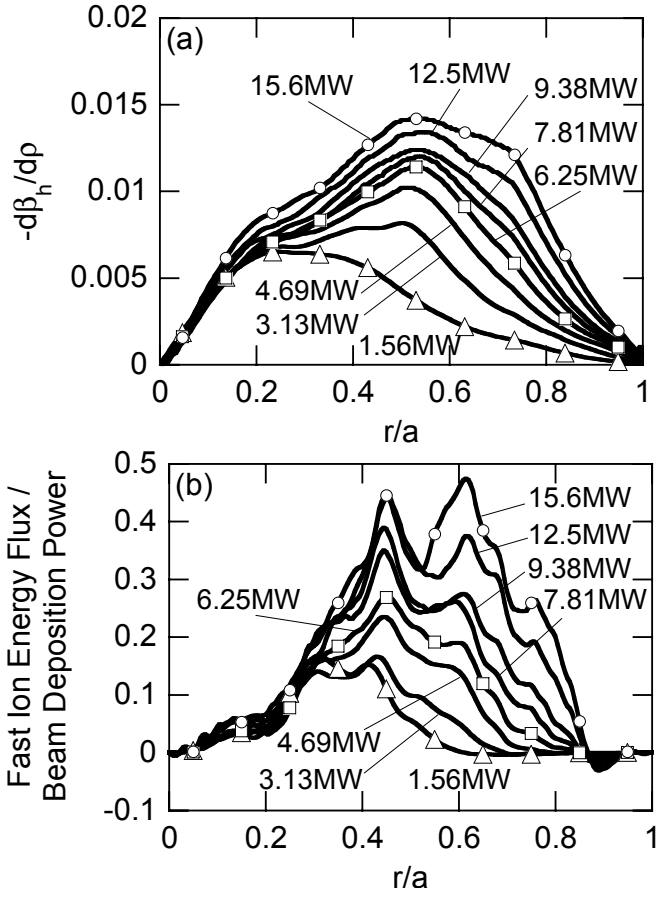

Figure 6. Radial profiles of (a) fast ion beta gradient and (b) fast ion energy flux normalized by the beam deposition power for various beam deposition powers. The fast ion beta profiles and the energy flux profiles are averaged in the last 2ms of the hybrid phase for each run. The fast ion energy flux is analyzed using Eq. (8) and summed over $n = 1 - 5$.

contribute to the fast ion transport, and the fluxes brought about by different modes are overlapped. This motivates us to investigate the resonance regions in fast ion phase space for each mode, and their overlap.

We analyze the resonance regions in fast ion phase space for a single eigenmode with fixed amplitude and frequency. The amplitude and frequency of the eigenmodes were analyzed for the last 2ms of the hybrid phase of each run. Figure 10 shows the particle trajectories in the phase space of normalized major radius $\hat{R} = (R - R_{axis})/(R_{edge} - R_{axis})$ and energy E [keV] for beam deposition power (a) 1.56MW, (b) 3.13MW, (c) 6.25MW, and (d) 15.6MW. The particle orbits were followed with the electromagnetic perturbations of a single eigenmode for 2ms, and the position in $(\hat{R}, E)$ space was recorded when the particle passes the mid-plane from bottom to top. Collisions are turned off to clarify the resonance regions. The particles are co-going to the plasma current with the same magnetic moment which gives $v_{\|}/v = 0.63$ for $E = 70$keV. The peak of the fast ion distribution is located at $v_{\|}/v = 0.63$. Only the particles trapped

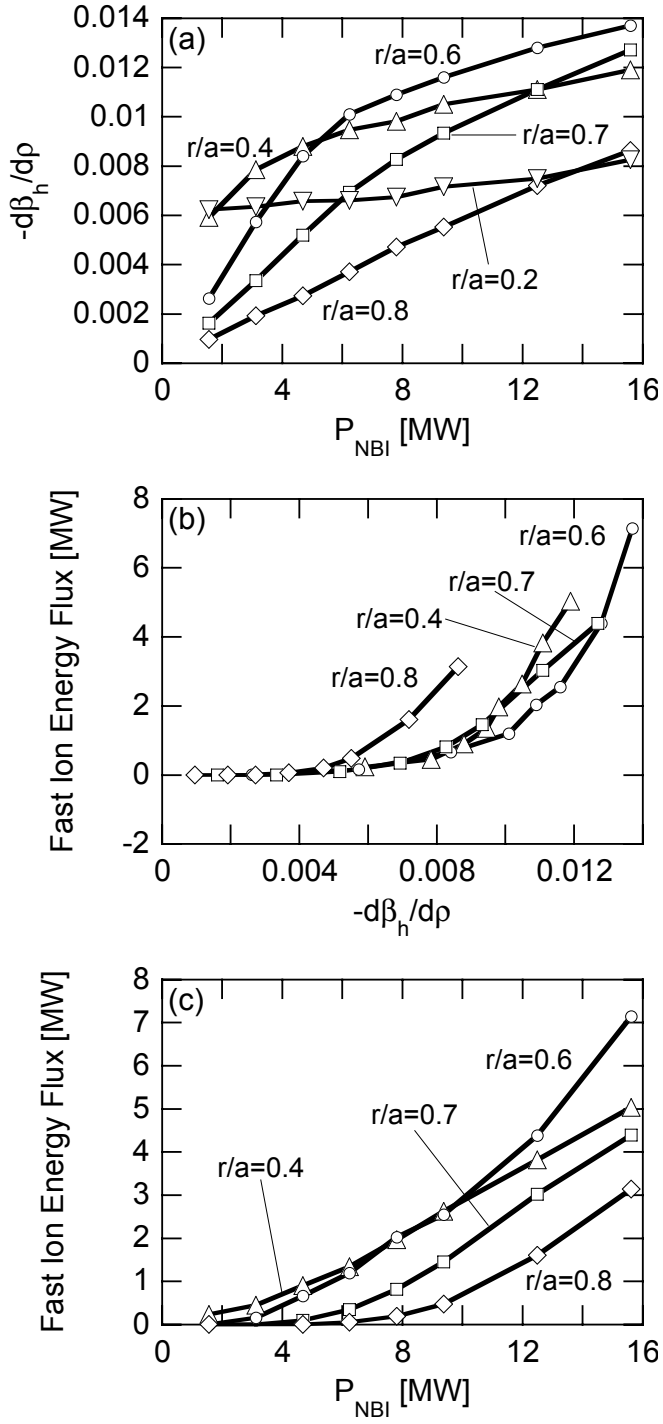

Figure 7. (a) Fast ion beta gradient versus beam deposition power, (b) fast ion energy flux versus fast ion beta gradient, and (c) fast ion energy flux versus beam deposition power for various radii.

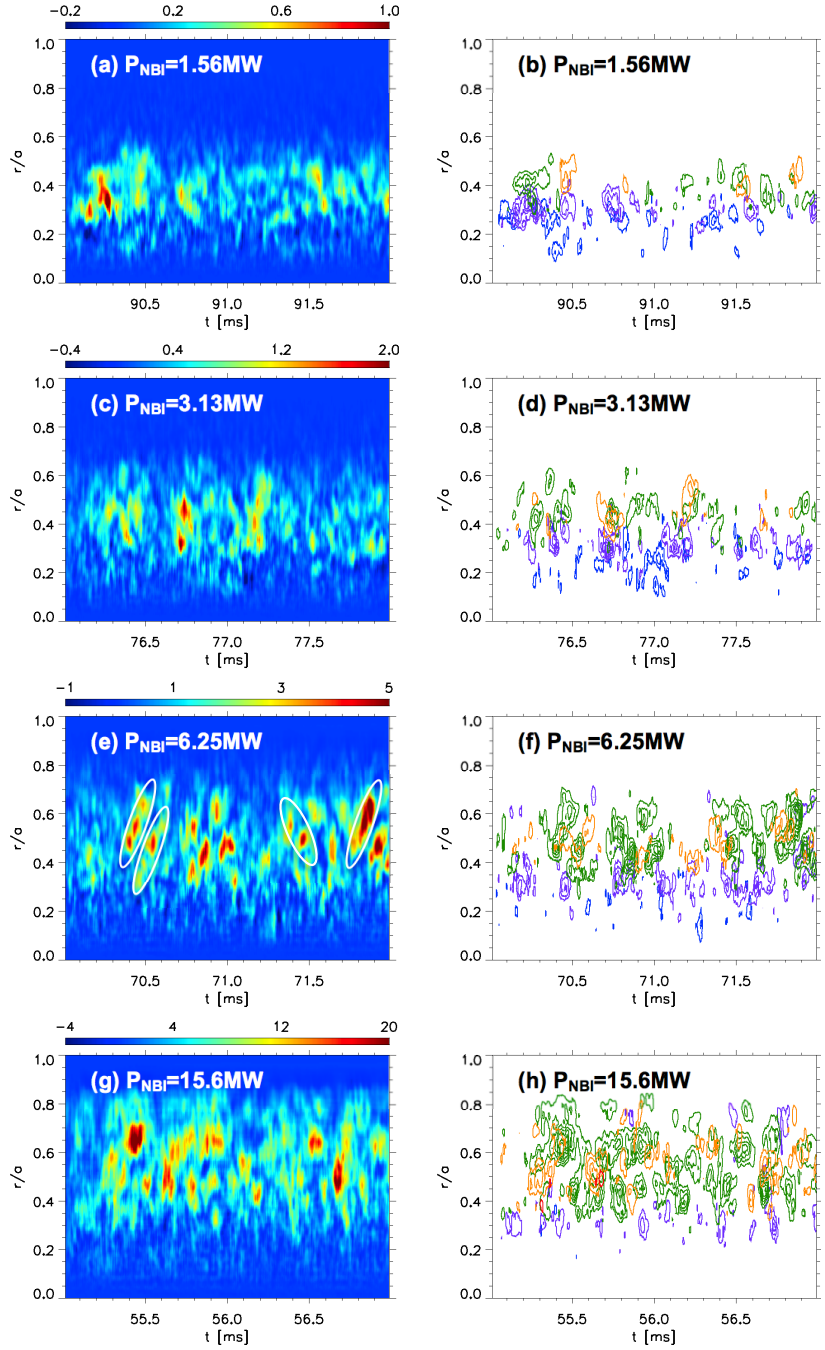

Figure 8. Time evolutions of fast ion energy flux profile and contours of the contributions from toroidal mode number $n = 1$ (blue), $n = 2$ (purple), $n = 3$ (green), $n = 4$ (orange), and $n = 5$ (red) for beam deposition power (a),(b) 1.56MW, (c),(d) 3.13MW, (e),(f) 6.25MW, and (g),(h) 15.6MW. The unit of the color bars in panels (a), (c), (e), and (g) is MW. Some avalanches are highlighted by white circle in panel (e).

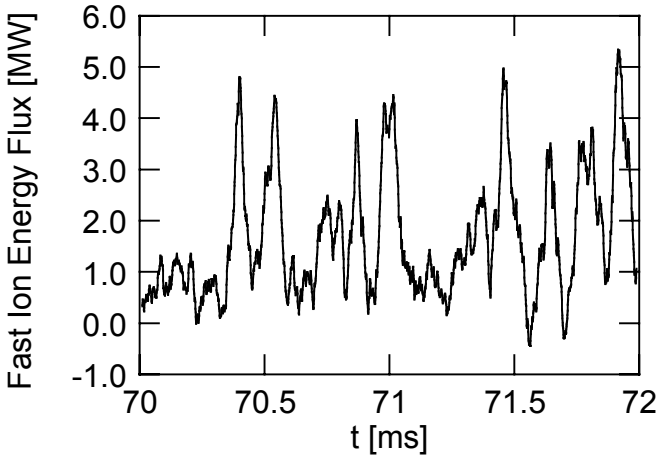

Figure 9. Time evolution of fast ion energy flux at $r/a = 0.46$ for beam deposition power 6.25MW.

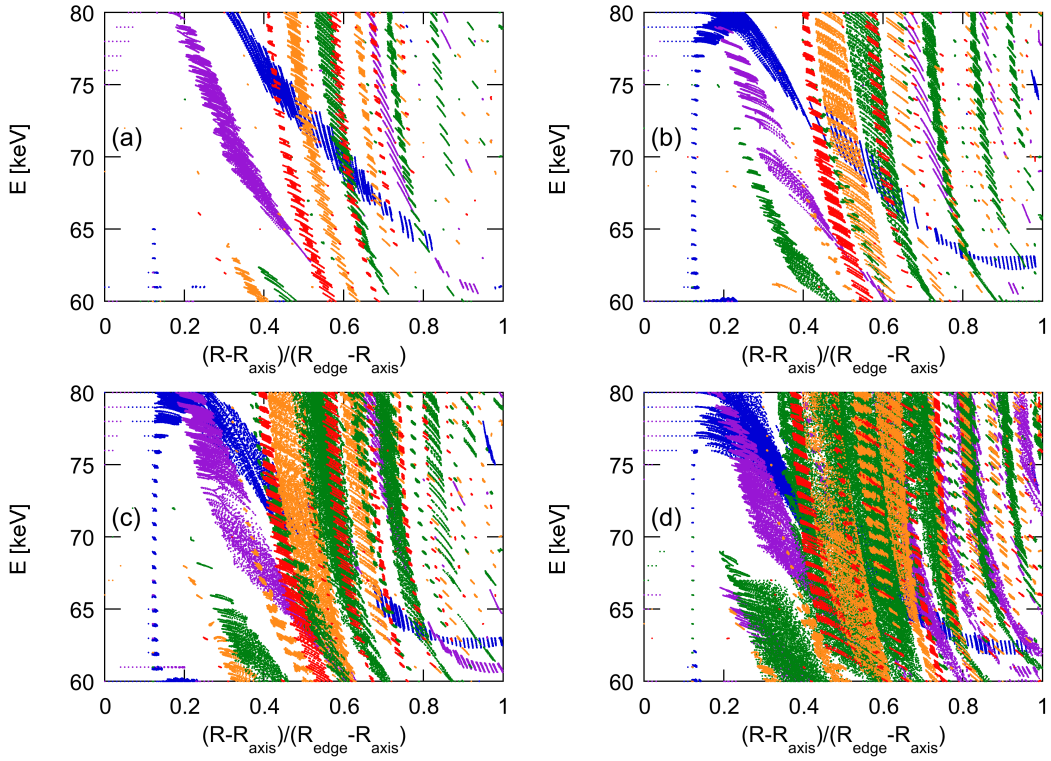

Figure 10. Particle trajectories in the phase space of normalized major radius $\hat{R} = (R - R_{axis})/(R_{edge} - R_{axis})$ and energy E [keV] for beam deposition power (a) 1.56MW, (b) 3.13MW, (c) 6.25MW, and (d) 15.6MW. Particle orbits are followed with the electromagnetic perturbations of a single TAE with fixed amplitude and frequency, and $\hat{R}$ and E are recorded when the particle passes the mid-plane from bottom to top. The particles are co-going to the plasma current with the same magnetic moment which gives $v_{\|}/v = 0.63$ for $E = 70$keV. Only the particles trapped by the TAE are plotted in the figure. The eigenmodes are represented by colors: $n = 1$ (blue), $n = 2$ (purple), $n = 3$ (green), $n = 4$ (orange), and $n = 5$ (red).

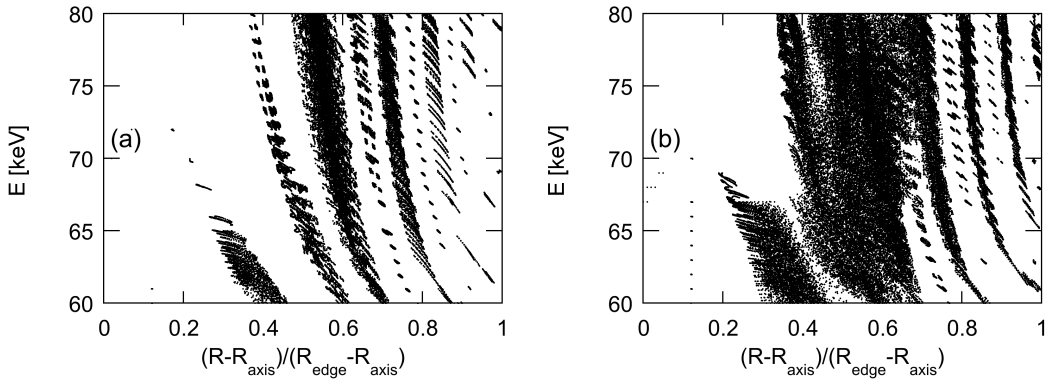

Figure 11. Particle trajectories in the phase space of normalized major radius $\hat{R} = (R - R_{axis})/(R_{edge} - R_{axis})$ and energy E [keV] for beam deposition power (a) 6.25MW and (b) 15.6MW. Particle orbits are followed with the electromagnetic perturbations of a single TAE with toroidal mode number $n = 3$, and $\hat{R}$ and E are recorded when the particle passes the mid-plane from bottom to top. The amplitude and frequency of the TAE are fixed. The particles are co-going to the plasma current with the same magnetic moment which gives $v_{\|}/v = 0.63$ for $E = 70$keV. Only the particles trapped by the TAE are plotted in the figure.

by the eigenmode are plotted in the figure. The time for this analysis (=2ms) is 1-30 times longer than the bounce period of the wave-particle trapping. The particles are initially located uniformly in $(\hat{R}, E)$ space with intervals 0.01 in horizontal axis and 1keV in vertical axis. The particles plotted can be regarded as resonance regions in phase space. The eigenmodes are represented by colors: $n = 1$ (blue), $n = 2$ (purple), $n = 3$ (green), $n = 4$ (orange), and $n = 5$ (red). Figure 10(d) for beam deposition power P_{NBI} =15.6MW contains a contribution from an additional $n = 2$ mode with frequency 57kHz, which is different from the $n = 2$ mode shown in Fig. 4(d) and located near the plasma edge. The readers are refferred to similar analyses for DIII-D [17] and AUG [34].

In Fig. 10(a) for P_{NBI} =1.56MW, only the resonance region of the $n = 1$ mode (blue) overlaps the resonance regions of the other modes, but the overlapped regions are small in the phase space. For P_{NBI} =3.13MW shown in Fig. 10(b), the resonance regions of $n = 2-5$ modes broaden due to the larger amplitude of eigenmodes. However, we see that gaps exist between the resonance regions of $n = 5$ (red), $n = 4$ (orange), and $n = 3$ (green) for $0.4 < \hat{R} < 0.6$. These gaps account for the normalized fast ion energy flux for P_{NBI} =3.13MW similar to that for P_{NBI} =1.56MW shown in Fig. 6(b). For P_{NBI} =6.25MW shown in Fig. 10(c), the resonance regions overlap substantially for $0.4 < \hat{R} < 0.6$. This is consistent with the enhanced fast ion energy flux for $0.4 < r/a < 0.6$ for P_{NBI} =6.25MW shown in Fig. 6(b). The overlapped region spreads outward up to $\hat{R} = 0.8$ for P_{NBI} =15.6MW shown in Fig. 10(d), which is also consistent with the fast ion energy flux profile shown in Fig. 6(b). This agreement between the fast ion energy flux profiles and the phase space structures indicates that the enhanced

fast ion transport can be attributed to the resonance overlap among the multiple Alfvén eigenmodes.

We have investigated the resonance overlap among the multiple Alfvén eigenmodes in Fig. 10. On the other hand, it has been pointed out that stochastic regions appear in phase space also for a single Alfvén eigenmode with large amplitude[35, 36, 37, 24]. Figure 11 compares the surface of section plots for $n = 3$ mode between P_{NBI} =6.25MW and 15.6MW. We see separate resonance regions for P_{NBI} =6.25MW in Fig. 11(a), and the overlap of the resonance regions for P_{NBI} =15.6MW in Fig. 11(b). This indicates that stochasticity appears for the single Alfvén eigenmode with large amplitude. The overlap of the resonance regions also accounts for the dominant amplitude of the $n = 3$ mode for P_{NBI} =15.6MW as shown in Fig. 5(a).

4. Discussion and summary

In this paper, we investigated the fast ion pressure profile flattened by multiple Alfvén eigenmodes for various neutral beam deposition powers with a multi-phase simulation, which is a combination of classical simulation and hybrid simulation for energetic particles interacting with a magnetohydrodynamic fluid. A monotonic degradation of fast ion confinement and the fast ion profile stiffness were found with increasing beam deposition power. The confinement degradation and the profile stiffness are caused by a sudden increase in fast ion transport flux brought about by Alfvén eigenmodes for the fast ion pressure gradient above a critical value. The critical pressure gradient and the corresponding beam deposition power depend on the radial location. The fast ion pressure gradient stays moderately above the critical value, and the profiles of the fast ion pressure and the fast ion transport flux spread radially outward from the inner region where the beam is injected. We found that the square root of the MHD fluctuation energy is proportional to the beam deposition power. We analyzed the time evolutions of the fast ion energy flux profiles, and found that intermittent avalanches take place with the contributions from the multiple eigenmodes. The surface of section plots demonstrated that the resonance overlap of multiple eigenmodes accounts for the sudden increase in fast ion transport with increasing beam power. The TAEs with $n = 1 - 5$ are observed for all the runs including the lowest beam deposition power. This indicates that the critical gradient and the critical beam power for the profile stiffness are substantially higher than the marginal stability threshold. The overlap of the resonance regions of a single TAE was also found for the largest beam power.

Some of the results summarized above are similar to the observations in DIII-D experiments [6] that studied discharges that are similar to but not identical to the discharges analyzed here. Similarities include: 1) sudden increase in fast ion transport above a critical beam power, 2) phase-space dependence of the critical beam power, 3) linear dependence of AE amplitude on beam power, and 4) intermittency in fast ion transport. On the other hand, we found a qualitative difference between the DIII-D experiments and the simulations. In the DIII-D experiments, the fast ion profiles do

not change above a critical beam power. This profile resiliency is not observed in the simulations presented in this paper. This difference can be attributed to the fast ion transport in the edge region. The fast ion transport does not reach the plasma edge where particles are lost, because the resonance overlap does not cover the whole phase space. There may be differences in the fast ion transport in the edge region and in the particle loss condition between simulation and experiment. In the experiments, the charge exchange with neutral particles and the micro turbulence [38] might affect the fast ion transport and losses in the edge region. A careful comparison in the fast ion transport in the edge region and the particle loss condition between simulation and experiment will be needed to understand the difference for the profile resiliency.

Acknowledgments

Numerical computations were performed at the Helios of the International Fusion Energy Center, the Plasma Simulator of the National Institute for Fusion Science, and the K Computer of the RIKEN Advanced Institute for Computational Science (Project ID: hp120212). This work was partly supported by MEXT as a priority issue to be tackeled by using Post 'K' Computer, JSPS KAKENHI Grant Number 15K06652, and the JSPS-NRF-NSFC A3 Foresight Program in the field of Plasma Physics (NRF: No. 2012K2A2A6000443, NSFC: No.11261140328).

Appendix A. Derivation of fast ion energy flux

The time evolution of the fast ion distribution function $f(\mathbf{x}, v_\parallel, v_\perp)$ in a conservative form is given by

$$\frac{\partial}{\partial t} f = -\nabla \cdot [(\mathbf{v}_E + v_\parallel \mathbf{b} + \mathbf{v}_B + \mathbf{v}_c) f] - \frac{\partial}{\partial v_\parallel}[\dot{v}_\parallel f] - \frac{\partial}{v_\perp \partial v_\perp}[v_\perp \dot{v}_\perp f], \quad \text{(A.1)}$$

where $\mathbf{v}_E$, $\mathbf{v}_B$, and $\mathbf{v}_c$ are $E \times B$, grad-B, and curvature drifts, respectively. We multiply Eq. (A.1) by $(v_\parallel^2 + v_\perp^2)/2$ and focus on the terms with $\mathbf{v}_E$ and $v_\parallel \mathbf{b}$ for the fast ion energy flux brought about by Alfvén eigenmodes:

$$\frac{1}{2}(v_\parallel^2 + v_\perp^2)\frac{\partial}{\partial t} f = -\nabla \cdot \left[\frac{1}{2}(v_\parallel^2 + v_\perp^2)(\mathbf{v}_E + v_\parallel \mathbf{b}) f\right] + (\text{other terms}). \quad \text{(A.2)}$$

We multiply Eq. (A.2) by fast ion mass m_h and integrate in velocity space to obtain

$$\frac{\partial}{\partial t}\frac{1}{2}(P_\parallel + 2P_\perp) = -\nabla \cdot \left[\frac{1}{2}\mathbf{v}_E(P_\parallel + 2P_\perp) + \frac{1}{2}\mathbf{b}(Q_\parallel + 2Q_\perp)\right] + (\text{other terms}), \quad \text{(A.3)}$$

$$P_\parallel = \int dv_\parallel \int 2\pi v_\perp dv_\perp m_h v_\parallel^2, \; P_\perp = \int dv_\parallel \int 2\pi v_\perp dv_\perp \frac{1}{2} m_h v_\perp^2,$$
$$Q_\parallel = \int dv_\parallel \int 2\pi v_\perp dv_\perp m_h v_\parallel^3, \; Q_\perp = \int dv_\parallel \int 2\pi v_\perp dv_\perp \frac{1}{2} m_h v_\parallel v_\perp^2.$$

The LHS of Eq. (A.3) is the time derivative of fast ion kinetic energy density. The fast ion energy flux $F(r)$ is given by integrating the RHS term inside the bracket [ ] on a magnetic surface labeled with r,

$$F(r) = \int_0^{2\pi} \mathcal{J}(r,\vartheta) d\vartheta \int_0^{2\pi} d\varphi \frac{1}{2} \left[(P_\parallel + 2P_\perp) \mathbf{v}_E \cdot \mathbf{n} + (Q_\parallel + 2Q_\perp) \mathbf{b} \cdot \mathbf{n} \right], \quad \text{(A.4)}$$

where $\mathcal{J}(r,\vartheta)$ is the Jacobian, and $\mathbf{n}$ is a unit normal vector to the magnetic surface. The net energy flux arises from the combinations of the fast ion moments $(P_\parallel, P_\perp, Q_\parallel, Q_\perp)$ and $\mathbf{v}_E$ and $\mathbf{b}$ with the same toroidal mode number n. We can define the fast ion energy flux brought about by the electromagnetic fluctuations with toroidal mode number n (Eq. (8)) by

$$F_n(r) = \int_0^{2\pi} \mathcal{J}(r,\vartheta) d\vartheta \int_0^{2\pi} d\varphi \frac{1}{2} \left[(P_{\parallel n} + 2P_{\perp n}) v_{Ern} + (Q_{\parallel n} + 2Q_{\perp n}) \delta b_{rn} \right], \quad \text{(A.5)}$$

where $v_{Er} = \mathbf{v}_E \cdot \mathbf{n}$ and $\delta b_r = \mathbf{b} \cdot \mathbf{n}$, and the subscript n indicates the toroidal mode number.

References

[1] FASOLI, A., GORMENZANO, C., BERK, H., et al., Nuclear Fusion **47** (2007) S264.
[2] HEIDBRINK, W. W., Phys. Plasmas **15** (2008) 055501.
[3] TOI, K., OGAWA, K., ISOBE, M., et al., Plasma Physics and Controlled Fusion **53** (2011) 024008.
[4] SHARAPOV, S., ALPER, B., BERK, H., et al., Nuclear Fusion **53** (2013) 104022.
[5] GORELENKOV, N., PINCHES, S., and TOI, K., Nuclear Fusion **54** (2014) 125001.
[6] COLLINS, C. S., HEIDBRINK, W. W., AUSTIN, M. E., et al., submitted to Phys. Rev. Lett. .
[7] GHANTOUS, K., GORELENKOV, N. N., BERK, H. L., HEIDBRINK, W. W., and VAN ZEELAND, M. A., Physics of Plasmas (1994-present) **19** (2012) 092511.
[8] BASS, E. M. and WALTZ, R. E., Physics of Plasmas (1994-present) **20** (2013) 012508.
[9] BERK, H. L., BREIZMAN, B., and PEKKER, M. S., Nuclear Fusion **35** (1995) 1713.
[10] HEIDBRINK, W. W., GORELENKOV, N. N., LUO, Y., et al., Phys. Rev. Lett. **99** (2007) 245002.
[11] VAN ZEELAND, M. A., HEIDBRINK, W., NAZIKIAN, R., et al., Nuclear Fusion **49** (2009) 065003.
[12] TOBIAS, B. J., CLASSEN, I. G. J., DOMIER, C. W., et al., Phys. Rev. Lett. **106** (2011) 075003.
[13] VAN ZEELAND, M. A., HEIDBRINK, W. W., FISHER, R. K., et al., Physics of Plasmas (1994-present) **18** (2011) 056114.
[14] VAN ZEELAND, M. A., GORELENKOV, N., HEIDBRINK, W., et al., Nuclear Fusion **52** (2012) 094023.
[15] TODO, Y., VAN ZEELAND, M. A., BIERWAGE, A., and HEIDBRINK, W., Nuclear Fusion **54** (2014) 104012.
[16] TODO, Y., ZEELAND, M. A. V., BIERWAGE, A., HEIDBRINK, W., and AUSTIN, M., Nuclear Fusion **55** (2015) 073020.
[17] WHITE, R. B., GORELENKOV, N., HEIDBRINK, W. W., and VAN ZEELAND, M. A., Plasma Physics and Controlled Fusion **52** (2010) 045012.
[18] WHITE, R. B., GORELENKOV, N., HEIDBRINK, W. W., and VAN ZEELAND, M. A., Physics of Plasmas (1994-present) **17** (2010) 056107.
[19] SPONG, D. A., CARRERAS, B. A., and HEDRICK, C. L., Physics of Plasmas (1994-present) **1** (1994) 1503.
[20] ZONCA, F., ROMANELLI, F., VLAD, G., and KAR, C., Phys. Rev. Lett. **74** (1995) 698.
[21] TODO, Y., BERK, H. L., and BREIZMAN, B. N., Nuclear Fusion **50** (2010) 084016.
[22] TODO, Y., BERK, H. L., and BREIZMAN, B. N., Nuclear Fusion **52** (2012) 033003.
[23] TODO, Y., BERK, H. L., and BREIZMAN, B. N., Nuclear Fusion **52** (2012) 094018.

[24] TODO, Y., BERK, H. L., and BREIZMAN, B. N., Physics of Plasmas (1994-present) **10** (2003) 2888.
[25] TODO, Y. and SATO, T., Physics of Plasmas (1994-present) **5** (1998) 1321.
[26] HAZELTINE, R. D. and MEISS, J. D., *Plasma Confinement*, Addison-Wesley Publishing Company, 1992.
[27] ZONCA, F. and CHEN, L., Phys. Rev. Lett. **68** (1992) 592.
[28] ROSENBLUTH, M. N., BERK, H. L., VAN DAM, J. W., and LINDBERG, D. M., Phys. Rev. Lett. **68** (1992) 596.
[29] METT, R. R. and MAHAJAN, S. M., Physics of Fluids B: Plasma Physics (1989-1993) **4** (1992) 2885.
[30] LITTLEJOHN, R. G., J. Plasma Phys. **29** (1983) 111.
[31] BIERWAGE, A., SHINOHARA, K., AIBA, N., and TODO, Y., Nuclear Fusion **53** (2013) 073007.
[32] BIERWAGE, A., TODO, Y., AIBA, N., and SHINOHARA, K., Nuclear Fusion **54** (2014) 104001.
[33] LAO, L., JOHN, H. S., STAMBAUGH, R., and PFEIFFER, W., Nuclear Fusion **25** (1985) 1421.
[34] SCHNELLER, M., LAUBER, P., BILATO, R., et al., Nuclear Fusion **53** (2013) 123003.
[35] HSU, C. T. and SIGMAR, D. J., Physics of Fluids B **4** (1992) 1492.
[36] SIGMAR, D. J., HSU, C. T., WHITE, R., and CHENG, C. Z., Physics of Fluids B **4** (1992) 1506.
[37] CANDY, J., BERK, H. L., BREIZMAN, B. N., and PORCELLI, F., Physics of Plasmas **6** (1999) 1822.
[38] ZHANG, W., LIN, Z., and CHEN, L., Phys. Rev. Lett. **101** (2008) 095001.